

Photometric and Spectral Evolution of the Symbiotic Nova HM Sagittae since 2003

N.P. Ikonnikova,^{1,*} V.I. Shenavrin,¹ G.V. Komissarova,¹ M.A. Burlak,¹ and A.V. Dodin¹

¹*Sternberg Astronomical Institute, M.V. Lomonosov Moscow State University, Moscow, 119234 Russia*

We present photometric and spectral monitoring of the symbiotic system HMsge, which consists of a Mira variable with a dust shell and a hot white dwarf ionizing the surrounding gaseous nebula. The system underwent a nova-like outburst in 1975 and experienced a high-activity episode during 2018–2021. *UBV* photometry from 2003 to 2025 shows monotonic fading at $\sim 0^m.05 \text{ yr}^{-1}$ until 2018, followed by a $0^m.3$ brightening peaking in 2021 and a decline by 2025 to the faintest level in five decades of monitoring. Near-infrared observations (*JHKLM*, 2009–2025), combined with archival data, reveal Mira pulsations with a period of 532 d and long-term variability driven by changes in the optical depth of the dust shell. Spectral monitoring (2016–2025) reveals a substantial evolution in the emission spectrum of the gaseous envelope. The 2018–2021 high-activity episode was accompanied by enhanced fluxes in recombination lines (H I, He I, He II) and forbidden transitions ([O I], [Ar V], [Fe VI], [Ca VII]), together with a 17-fold brightening of the Raman-scattered O VI $\lambda 6725$ line. We report the first detection of the [Fe X] $\lambda 6374$ line in HMsge. Monitoring this line from 2007 to 2025 shows its equivalent width growing through 2017 – indicating gradual coronal heating – then declining by 2021, likely reflecting altered accretion conditions and/or hot-component properties during the high-activity episode. We propose that both the 1975 outburst and the 2018–2021 high-activity episode may be linked to periastron passage of the binary components; if so, the ~ 46 -year interval would constrain the system’s orbital period.

Keywords: stars – symbiotic novae – photometry, spectra, HMsge

1. INTRODUCTION

Symbiotic novae constitute a unique class of interacting binary systems in which a thermonuclear explosion on the surface of an accreting white dwarf (WD) leads to a long-lasting (from several decades to centuries) and substantial increase in luminosity. Investigation of the long-term post-outburst evolution provides essential insights into mass-loss mechanisms, the stability of nuclear burning, and the physical conditions within the complex multi-component environment surrounding the binary system.

Only about ten confirmed objects in the Galaxy are known to have exhibited nova-like outbursts over the past century and a half. Among the most prominent and well-studied are V1016 Cyg, V1329 Cyg, AG Peg, and RR Tel. HMsge occupies a special place among such objects – a D-type (Dusty) symbiotic system according to the classification of Allen (1984), containing a Mira-type variable surrounded by a dust shell. Fifty years ago, in 1975, this sys-

tem underwent a powerful nova-like outburst (Dokuchaeva 1976), which brought it out of quiescence and established it as one of the primary targets for studying the late evolutionary stages of symbiotic novae.

Subsequent decades of observations have made it possible to trace in detail the gradual fading of the outburst and the evolution of the system’s physical parameters. However, in the late 2010s, HMsge once again exhibited signs of increased activity. Observations from 2018–2021 recorded a brightening and spectral changes indicative of a possible resumption of thermonuclear activity, a change in the accretion regime, or a large-scale restructuring of the circumstellar environment. This event, which occurred half a century after the main outburst, raises fundamental questions about the nature of the late evolutionary stages of symbiotic novae, the mechanisms of outburst recurrence, and the long-term stability of nuclear burning on WDs.

In this work, we present a comprehensive analysis of observational data for HMsge, covering both the entire 50-year period since the 1975 outburst and the recent activity of 2018–

* ikonnikova@gmail.com

2021. Using new photometric and spectral observations, supplemented by archival data, we investigate the evolution of the ionized nebula and dust shell surrounding the system.

Some key parameters of the system are summarized in Table 1.

2. *UBV* OBSERVATIONS

The results of *UBV* observations of HMSge obtained prior to 2002 have been published previously (Arkhipova et al. 1994, 2004). In recent years, new observations have been carried out using the same 60-cm reflector at the Crimean Astronomical Station (CAS) of SAI MSU, equipped with the photometer designed by V.M. Lyutyj (Lyutyj 1971) and operating in the same photometric system. Observations were performed using a 13'' diaphragm to exclude the contribution of a faint companion located 8'' north of HMSge. As in previous studies, BD+16°3965 (spectral class F5) was used as the comparison star. The magnitudes of the comparison star were adopted as $V = 10^m.70$, $B = 11^m.33$, and $U = 11^m.48$ (Arkhipova et al. 1994). Our *UBV* observations of HMSge from 2003 to 2025 are presented in Table A1. We estimate the photometric precision to be $0.^m01 - 0.^m02$ in the V and B bands, and no worse than $0.^m03$ in the U band.

3. *JHKLM* OBSERVATIONS

JHKLM photometry of HMSge has been carried out on the CAS SAI MSU 1.25-m telescope since 1978. Infrared (IR) flux measurements were carried out using an InSb photometer developed and built in the early 1980s (Nadjip et al. 1986). A detailed description of the observing technique and data reduction is given in Shenavrin et al. (2011). The star BS 7488 from the catalog of Johnson et al. (1966) is used as the photometric standard. The angular diameter of the exit diaphragm is approximately 12'', and the spatial beam separation during modulation is $\sim 30''$ in the east–west direction. Measurement uncertainties do not exceed $0.^m01$ in the J , H , K , and L bands, and $0.^m02$ in the

M band. The results of *JHKLM* photometry from 1978 to 2008 have been published in Shenavrin et al. (2011), Taranova and Shenavrin (2000), Taranova and Yudin (1983), Yudin et al. (1994), Yudin (1994). Our near-IR observations obtained during 2009–2025 are presented in Table A2.

4. SPECTROSCOPIC OBSERVATIONS

Spectroscopic observations of HMSge during 2016–2025 have been carried out on the CAS SAI MSU 1.25-m telescope using the low-resolution spectrograph (A-sp) designed by V.F. Esipov, with a 600 lines mm^{-1} diffraction grating, a 4''-wide long slit, $\text{FWHM} \sim 7 \text{ \AA}$, and a spectral range of 4000–10000 \AA . The following detectors were used: the SBIG ST-402 CCD (765×510 pixels) in 2016–2017, the FLI PL-4022 (2048×2048 pixels) in 2021, and the CMOS camera ASI2600MM/MC Pro (6248×4176 pixels) in 2024–2025. Spectroscopic observations of HMSge on the same telescope during 2003–2016 were also obtained; however, due to issues with absolute flux calibration of spectra, we present only equivalent widths for that period.

In 2021 and 2025, additional spectroscopic observations of HMSge were obtained on the CMO SAI MSU 2.5-m telescope using the low-resolution Transient Double-beam Spectrograph (TDS) equipped with holographic gratings (Potanin et al. 2020). Andor Newton 940P cameras with E2V CCD42-10 detectors (512×2048 pixels) were used. Observations were performed with a long slit of width 1.''0 or 1.''5. The covered spectral range is 3500–7500 \AA , with spectral resolving power $R \approx 1300$ in the blue channel (3500–5720 \AA) and $R \approx 2500$ in the red channel (5720–7500 \AA). Data reduction was performed using custom Python scripts; the procedure is described in detail in Potanin et al. (2020).

The log of spectroscopic observations is presented in Table 2.

Table 1. Key parameters of the symbiotic nova HM Sge.

Parameter	Value	Reference
Coordinates and distance:		
Right Ascension (RA, J2000)	19 ^h 41 ^m 57.1 ^s	Gaia Collaboration et al. (2021)
Declination (Dec, J2000)	+16°44′39.8″	Gaia Collaboration et al. (2021)
Distance	1035 ⁺¹¹⁸ ₋₁₀₂ pc	Bailer-Jones et al. (2021)
Mira-type star (cool companion):		
Spectral class	M7	Mürset and Schmid (1999)
Luminosity	~ 1000 L_{\odot} 1500 – 2000 L_{\odot}	Taranova and Shenavrin (2000) Goldman et al. (2024)
Radius	~ 540 R_{\odot}	Taranova and Shenavrin (2000)
Temperature	2400–3000 K	Taranova and Shenavrin (2000)
Mass-loss rate (gas)	~ 4 × 10 ⁻⁶ M_{\odot} yr ⁻¹	Goldman et al. (2024)
Pulsation period	535 ± 5 days	Taranova and Shenavrin (2000)
Pulsation amplitude (ΔJ)	~ 1. ^m 0	Taranova and Shenavrin (2000)
White dwarf (hot component):		
Temperature (2021)	> 250 000 K	Goldman et al. (2024)
Dust shell:		
Radius	~ 1500 R_{\odot}	Taranova and Shenavrin (2000)
Mass	4 – 8 × 10 ⁻⁵ M_{\odot}	Taranova and Shenavrin (2000)

Table 2. Log of spectroscopic observations.

Date	JD-2400000	Instrument	Standard
2016-07-30	57600.46	A-sp	HD 353437
2017-07-01	57936.45	A-sp	HD 353437
2021-06-10	59376.45	TDS	BD+33° 2642
2021-07-15	59411.33	A-sp	HD 353437
2021-09-09	59467.33	A-sp	HD 353437
2024-07-07	60499.41	A-sp	HD 353437
2025-05-04	60800.47	TDS	HIP 87939
2025-08-14	60902.38	A-sp	HD 353437
2025-11-18	60998.18	TDS	HIP 106758

5. PHOTOMETRIC EVOLUTION

5.1. Optical range

The light curves covering the entire period of UBV observations are shown in Fig. 1, which displays the annual mean magnitudes for 1976–2002 from Arkhipova et al. (2004) and new data obtained during 2003–2025. As noted previously (Arkhipova et al. 1994), the mean brightness in all three bands remained constant from 1977 to 1982, with fluctuations of amplitude $\sim 0.^m1$, followed by a brightening in the U band. HM Sge remained in this “high” state for approximately 7 years, and starting in 1989, a systematic fading

occurred at a rate of $\sim 0.^m05$ yr⁻¹ until 2017. In the B and V bands after 1982, the brightness declined monotonically at approximately the same rate as in the U band. Intra-seasonal brightness variations did not exceed $0.^m1$ – $0.^m2$.

In 2018, the brightness of HM Sge began to increase in all observed bands, reaching a maximum in 2021 with an amplitude of $\sim 0.^m3$ relative to the 2017 level. In subsequent years, a monotonic fading was observed, and by 2025 the brightness reached the minimum values recorded in the last 50 years. If the fading trend observed before 2018 were extrapolated, the expected brightness level in 2025 would have been higher than observed. This indicates that the 2018–2021 event significantly changed the state of the system, preventing the hot star and its ionized envelope from returning to the pre-brightening state.

Previously, the behavior of HM Sge in the $(B-V)$, $(U-B)$ two-color diagram was discussed in Arkhipova et al. (1994, 2004). Here we present an updated two-color diagram (Fig. 2), extended with observations from the last two decades. In recent years, the previously identified trend has persisted: the star continues to shift toward bluer $(U-B)$ values while simultaneously reddening in

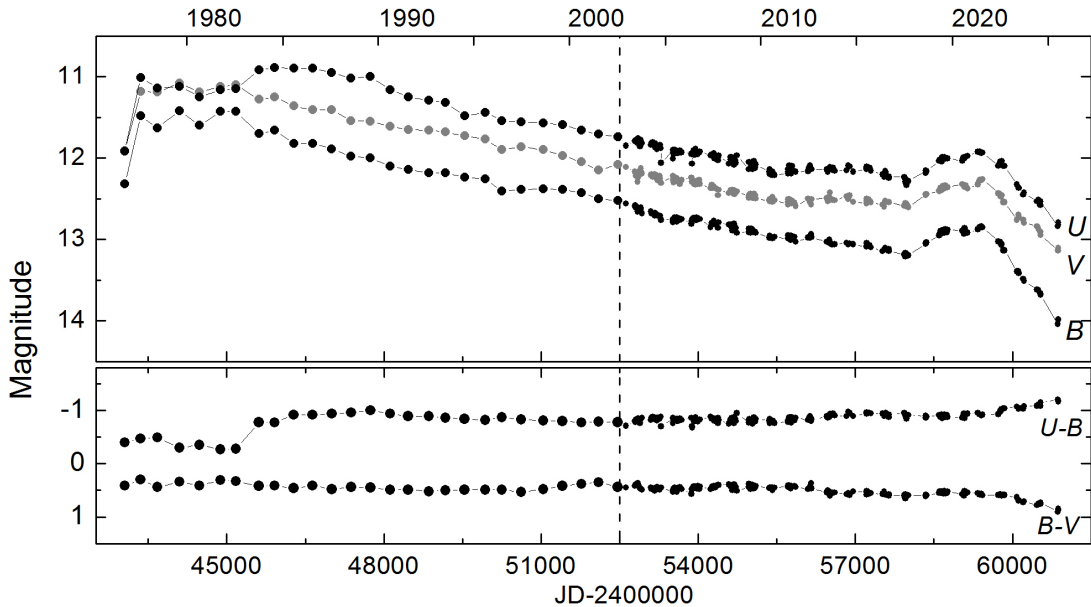


Figure 1. Light and color curves of HM Sge from 1976 to 2025. New data are shown to the right of the vertical dashed line.

($B-V$). As in previous studies, we attribute this motion in the diagram to changes in the parameters of the gaseous envelope, which remains the dominant source of emission in the UBV photometric bands. The contributions of both the hot star and the cool component (the Mira variable) are substantially smaller in this spectral region. As will be shown below (see the section on spectral evolution), the emission-line spectrum of the system has undergone significant changes, further confirming the dynamic nature of the observed processes.

5.2. Near-IR range

Figure 3 presents the light curves of HM Sge in the $JHKLM$ bands from 1978 to 2025. New data from 2009–2025 are shown to the right of the vertical dashed line. Earlier observations are taken from Shenavrin et al. (2011), Taranova and Shenavrin (2000), Taranova and Yudin (1983), Yudin et al. (1994), Yudin (1994). The time interval during which optical brightening was recorded is highlighted in the figure. It can be seen that only in the J band did the brightness increase slightly during this period.

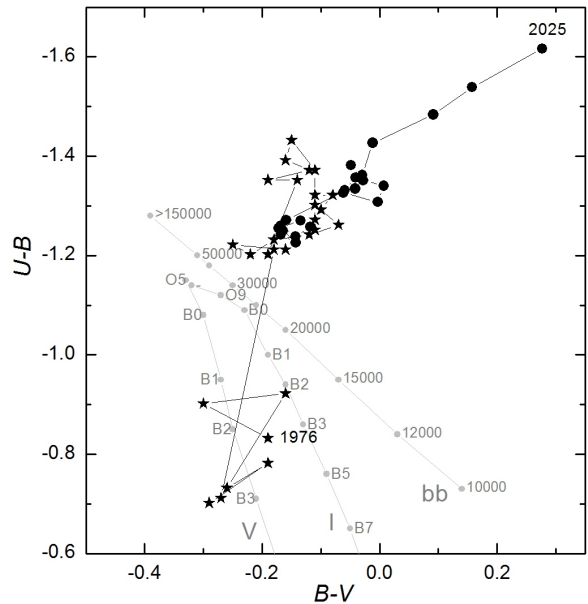


Figure 2. Motion of HM Sge in the two-color diagram. Annual mean values are shown, corrected for interstellar extinction with $E(B-V) = 0.6$. Years are indicated by numbers. Data from 1976–2002 are shown as stars, and from 2003 to 2025 as circles. Gray lines show the loci of blackbody radiation (bb), main-sequence stars (V), and supergiants (I).

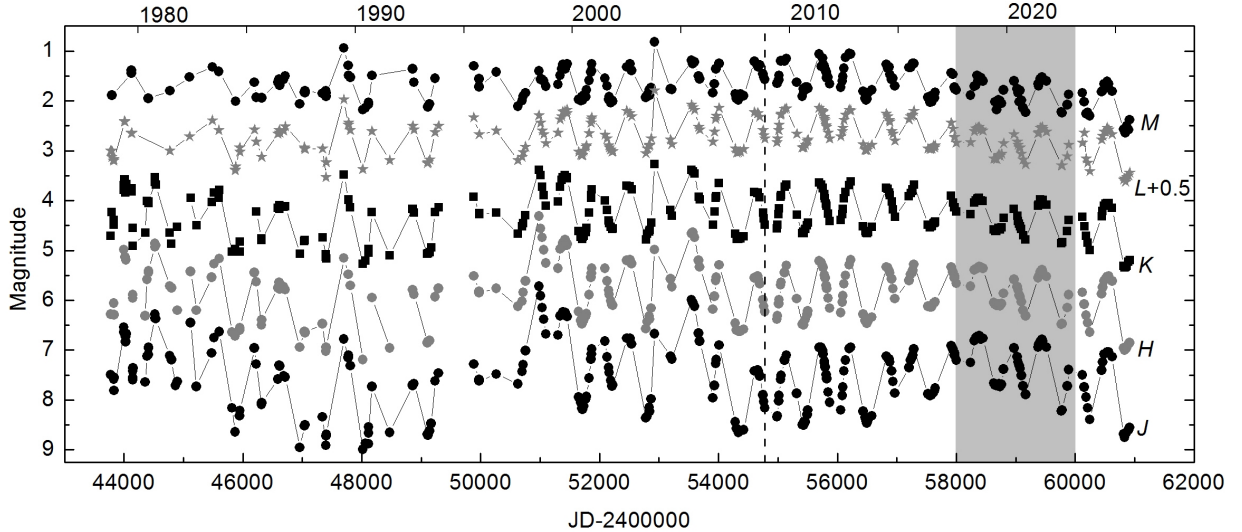


Figure 3. Light curves in the $JHKLM$ bands from 1978 to 2025. New data are shown to the right of the vertical dashed line. The period of optical brightening is highlighted in gray.

The star exhibits stable periodic variations superimposed on a long-term non-monotonic trend. The peak-to-peak amplitudes of periodic variations in different photometric bands are: $\Delta J = 1.^m4$, $\Delta H = 1.^m2$, $\Delta K = 0.^m95$, $\Delta L = 0.^m8$, and $\Delta M = 0.^m7$. Figure 4 shows the periodogram constructed from the J -band data spanning 1978–2025. The derived period $P = 532 \pm 5$ days agrees well (within uncertainties) with the value obtained previously from a shorter time series (Taranova and Shenavrin 2000).

In addition to periodic brightness variations, slow variations with characteristic timescales of several thousand days have been detected in the near-IR range. The most pronounced trend is observed in the J band, which may be related to changes in the optical depth of the star’s dust shell. According to Taranova and Shenavrin (2000), following the 1975 outburst of the hot component, the dust shell reached maximum density approximately 13 years later (around JD 2447500), after which its gradual dispersal began. By JD 2451000, the J -band brightness reached a maximum and then started to decline until JD 2454500; after this date, the mean brightness began to increase again. Another decline in mean brightness is observed following the 2018–2021 event. Early observations

in 2025 show that the star’s brightness has decreased in all NIR bands to the level of the early 1990s, when the dust shell was at its maximum density. One might hypothesize that a dust-formation episode occurred in the system, associated with a weak recurrent outburst; however, the expected reddening of color indices was not observed. Figure 5 shows the light curve in the J band and the $J - H$, $K - L$, and $L - M$ color curves for the recent period from 2008 to 2025. Long-term brightness variations are fitted with a quadratic polynomial. The $J - H$ color index exhibits bluer values starting in 2018 (the onset of optical brightening), while the J -band brightness fades. The color indices $K - L$ and $L - M$ have not undergone significant changes.

The $(J - K)$ vs. J color–magnitude diagram (Fig. 6) is of particular interest. Recent observations clearly separate into two temporal groups: 2008–2018 and 2019–2025. Within each group, the star reddens as it fades during pulsations; however, the mean color index has become bluer in 2019–2025, indicating that the system parameters changed during and after the high-activity episode.

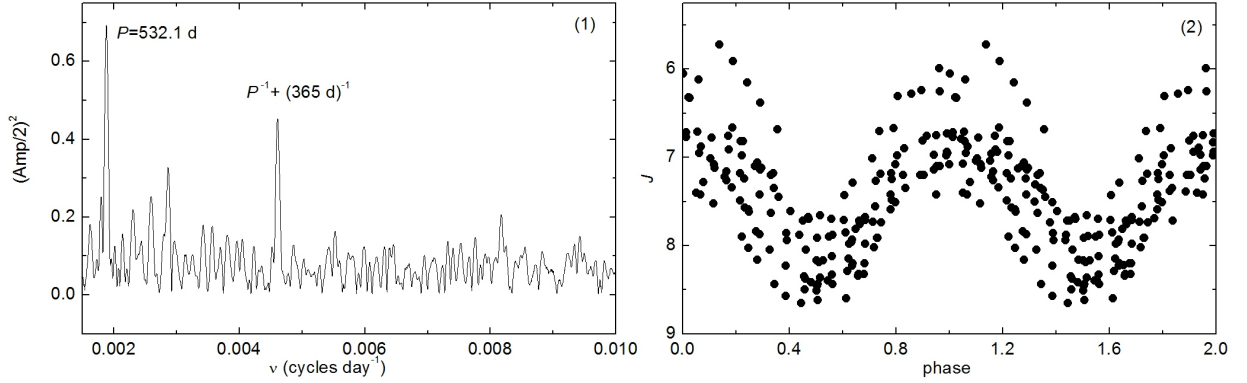


Figure 4. Periodogram of the J -band time series (1) and the corresponding phase-folded light curve with $P = 532.1$ d (2), based on the complete 1978–2025 dataset.

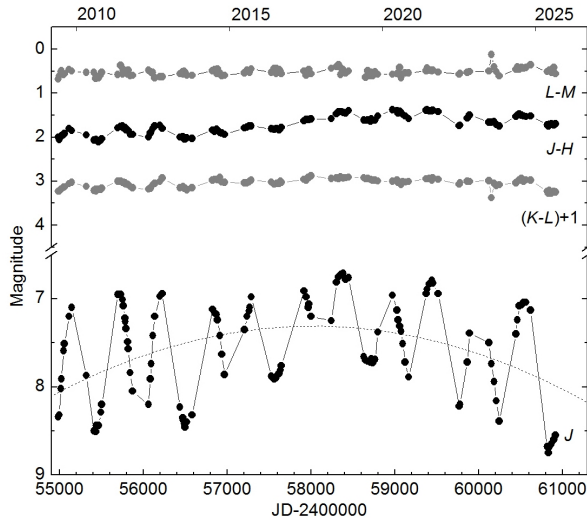


Figure 5. Light and color curves from 2008 to 2025. The dashed line shows a second-order polynomial fit.

6. SPECTRAL EVOLUTION

Over half a century of observations, the optical spectrum of the symbiotic nova HM Sge has undergone significant changes, reflecting the evolution of its hot component. The variable flux of ionizing radiation has affected the state of the surrounding gaseous envelope, which is the dominant source of emission in the optical range. The spectrum was studied most extensively during the first two decades after the 1975 outburst. Thus, monitoring results from 1976 and 1977 are presented in Ciatti et al. (1977, 1978), and

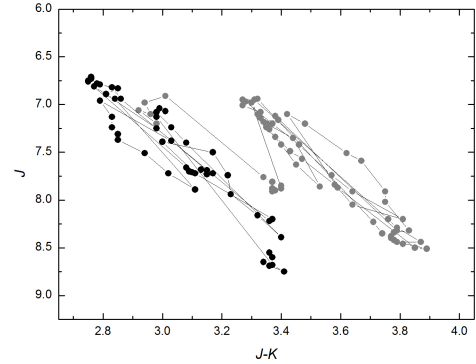


Figure 6. Color-magnitude diagram ($(J - K)$ vs. J) for 2009–2025. Gray points show data from 2008–2017; black points show data from 2018–2025.

the evolution of the emission-line spectrum from 1977 to 1982 was traced by Stauffer (1984). Data from 1985–1986 were summarized by Pacheco et al. (1989), and observations from 1987 were analyzed by Schmid and Schild (1990). In addition, analysis of spectra from individual epochs is contained in Arkhipova et al. (1979), Blair et al. (1981), Brown et al. (1978), Davidson et al. (1978), Ipatov and Yudin (1981), Puetter et al. (1978), Shanin (1978). A brief review of spectroscopic observations during the first decade after the outburst is presented in Nussbaumer and Vogel (1990). Later observations are reported in a series of papers (Arkhipova et al. 1994, 2004, Arkhipova and Noskova 1991, Noskova 1996). Here we analyze new spectroscopic observations

of H M Sge obtained during 2016–2025 and compare them with previously published data.

The observed optical spectrum of H M Sge represents a complex superposition of emission components arising from regions with vastly different physical conditions. The spectrum is rich in emission lines. The most intense among them are hydrogen Balmer series lines, forbidden [O III] lines, He II lines, and highly ionized [Fe VII] lines. Weaker lines of He I, [O I], [O II], [N II], [S II], [S III], [Ar III], [Ar V], [Ca V], and [Fe VI] are also observed. Such a spectrum is characteristic of a gaseous nebula excited by radiation from a high-temperature source. In the red spectral region ($\lambda > 6000 \text{ \AA}$), the continuum of the red component (the Mira variable) is present, with the intensity varying significantly depending on the pulsation cycle phase (Arhipova et al. 2004).

In the first years after the 1975 outburst, the most significant changes in the emission-line spectrum of H M Sge were observed during a 10-month interval beginning in August 1979, as described in detail by Stauffer (1984). Before August 1979, the effective temperature of the hot component was below 70 000 K, and the spectrum showed signatures of a high-velocity wind – Wolf–Rayet bands and broad Balmer line wings. By May 1980, the temperature of the hot star had increased to $\sim 160\,000$ K, the wind had virtually disappeared, and [Fe VII] lines appeared in the spectrum.

In the following decades, the absolute fluxes of nearly all emission lines gradually declined (Arhipova et al. 2004, Arhipova and Noskova 1991, Mürset and Nussbaumer 1994). Such fading is characteristic of symbiotic novae and is a natural consequence of the cooling, expansion, and recombination of the ejected envelope. This process spans decades, consistent with the characteristic timescales of cooling and expansion in the dense environment of symbiotic systems. The temperature of the hot star continued to rise, reaching $\sim 200\,000$ K by 1992 (Mürset and Nussbaumer 1994). Goldman et al. (2024) reported that the temperature of the hot component, based on ultraviolet spectroscopic observations from 2021, exceeds 250 000 K, derived from the flux ratio of the [Ne V] $\lambda 1575$ and [Ne IV] $\lambda 1601$ lines.

The 2018–2021 high-activity episode dramatically altered the emission-line spectrum, disrupting the long-term spectral evolution.

6.1. Variation of absolute emission-line fluxes

Observations from 2016 revealed a decline in fluxes of nearly all measured emission lines compared to the data from Arhipova et al. (2004) for 1994–2002. The only exception was the Raman-scattered O VI $\lambda 6825$ line, whose flux remained almost unchanged relative to the 2002 measurements. The degree of line fading varied depending on the ion. Thus, the H β and He II lines faded by a factor of ~ 2.4 . The nebular [O III] $\lambda\lambda 4959, 5007$ lines weakened by a factor of ~ 3.5 , while the auroral [O III] $\lambda 4363$ and [N II] $\lambda 5755$ lines faded by more than a factor of 4. The [S II] $\lambda 6716$ and $\lambda 6731$ lines proved most stable, showing minimal fading. At the same time, the flux of the [S III] $\lambda 6312$ line decreased by nearly a factor of 4. The He I $\lambda\lambda 5876, 6678, \text{ and } 7065$ lines became weaker by a factor of 2–2.5.

Our spectroscopic observations have allowed us to trace the evolution of emission-line fluxes during 2016–2025, a period that covered the phases before, during, and after the 2018–2021 high-activity episode. Tables A3 and A4 present absolute line fluxes measured from spectra obtained with the CAS SAI MSU 1.25-m and CMO SAI MSU 2.5-m telescopes. Figure 7 shows the evolution of absolute fluxes for selected emission lines from 2016 to 2025 based on our new observations, together with *B*- and *V*-band light curves for the same period.

The H β flux increased by a factor of 1.4 from 2016 to 2021, then began to decline and by 2025 reached its minimum value throughout the history of spectroscopic observations of H M Sge – $\sim 3 \times 10^{-12} \text{ erg cm}^{-2} \text{ s}^{-1}$. The He II $\lambda 4686$ line showed similar behavior: its absolute flux increased from 2016 to 2021 and then decreased by 2025. The maximum luminosity of the hot component during the outburst led to the highest degree of ionization and, consequently, to the maximum intensity of recombination lines and

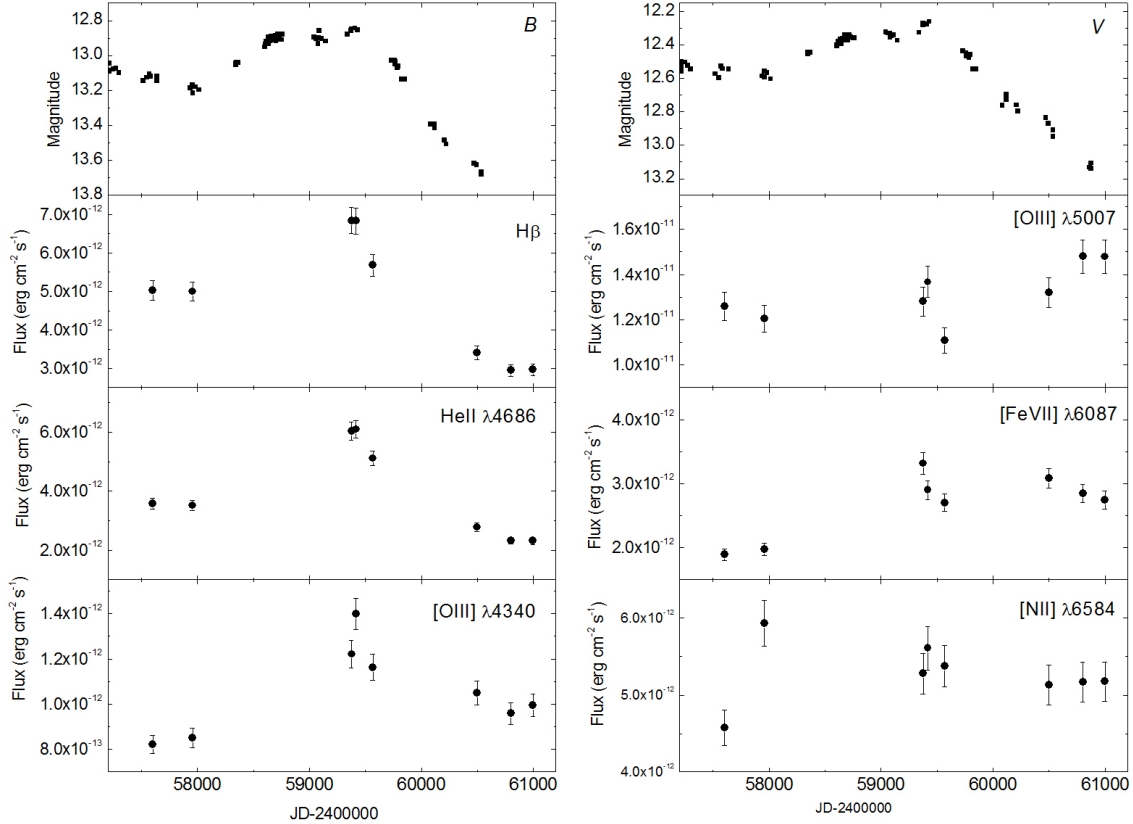


Figure 7. Evolution of absolute fluxes for selected emission lines from 2016 to 2025, together with *B*- and *V*-band light curves.

high-excitation lines. In addition, we note the presence of broad $H\alpha$ wings in the 2021 spectrum and their absence in 2025. The flux of the auroral $[O\text{ III}] \lambda 4363$ line increased by a factor of 1.7 from 2016 to 2021, then began to decline; in 2025, it remained slightly higher than in 2016. A different pattern was observed for the nebular lines $[O\text{ III}] \lambda 5007$ and $[N\text{ II}] \lambda 6584$. The $[O\text{ III}] \lambda 5007$ line showed little response to the outburst, but its flux increased slightly afterward. Presumably, the ionization wave from the outburst reached more distant and diffuse regions of the envelope, where this line forms efficiently. The $[N\text{ II}] \lambda 6584$ line showed relative stability: its flux did not experience significant enhancement during the photometric maximum of the star. This is consistent with the view that its formation region during this period was only weakly affected by processes related to the outburst.

Lines showing behavior similar to $H\beta$ include $\text{He I } \lambda\lambda 4471, 5876, 6678, 7065$, $\text{He II } \lambda 5412$, and the forbidden lines $[O\text{ I}] \lambda\lambda 6300, 6364$, $[\text{Ar V}] \lambda\lambda 6435, 7006$, $[\text{Fe VI}] \lambda 5158$, and $[\text{Ca VI}] \lambda 5716$. The high-excitation lines $[\text{Fe VII}] \lambda\lambda 5721, 6087$ increased in strength by 2021 and maintained enhanced intensity through 2025. For the first time in the history of observations of HM Sge, the $[\text{Fe X}]$ line was detected, whose emergence and evolution is described in Section 6.1.2. The $[O\text{ II}] \lambda\lambda 7320, 7331$ doublet showed little response to the episode: the combined flux of these lines gradually declined from 2016 to 2025. Significant enhancement during the high-activity episode was exhibited by the permitted $\text{Fe II } \lambda\lambda 4657, 5317, 5535, 6417, 6455$ lines.

Figure 8 compares the spectrum of HM Sge at two epochs: June 6, 2021, and November 18, 2025. Characteristic emission lines are labeled.

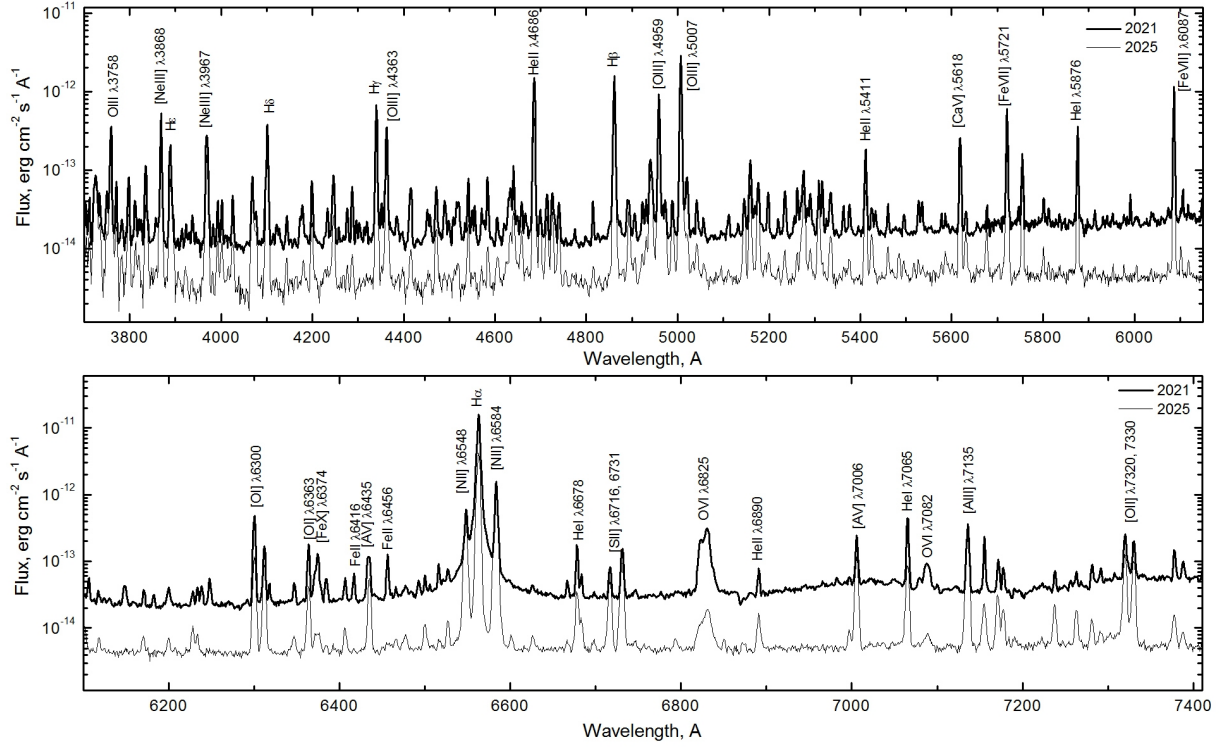


Figure 8. Spectra of HM Sge from June 6, 2021 (thick line) and November 18, 2025 (thin line).

6.1.1. Raman-scattered O VI lines

The most significant changes during the 2018–2021 event affected the broad emission features in the optical spectral range – the $\lambda 6825$ and $\lambda 7082$ lines, which are produced by Raman scattering of the O VI resonance doublet ($\lambda\lambda 1032, 1038$) by neutral hydrogen (H I).

In the 1987 spectrum (Schmid and Schild 1990), as in previous observations, these lines were not detected. The $\lambda 6825$ line was first measured in Arkhipova et al. (2004) from spectra obtained during 1994–2002. That work also notes that this line was present in an echelle spectrum from 1992. Lee and Kang (2007) presented and analyzed the profile of the O VI $\lambda 6825$ line obtained in 2005. The authors modeled the $\lambda 6825$ line profile using a Monte Carlo method, assuming that the O VI emission region is a Keplerian accretion disk around the hot component, while scattering occurs in the slow spherical wind from the Mira variable. Analysis of 2014 observations and modeling of both Raman-scattered O VI lines at $\lambda 6825$ and $\lambda 7082$ are presented in Lee et al.

(2016). That study showed that the flux ratio $F(\lambda 6825)/F(\lambda 7082)$ of the Raman-scattered lines is a sensitive indicator of the neutral hydrogen column density N_{HI} in the scattering region. Observations of HM Sge in 2014 yielded a flux ratio corresponding to $N_{\text{HI}} \sim 10^{22} \text{ cm}^{-2}$, which is typical of widely separated D-type symbiotic stars.

Figure 9 shows the evolution of the absolute flux of the Raman-scattered O VI $\lambda 6825$ line from 2016 to 2025 based on our new spectroscopic observations. Compared to the September 2002 measurement from Arkhipova et al. (2004) ($F(\lambda 6825) = (1.9 \pm 0.6) \times 10^{-13} \text{ erg cm}^{-2} \text{ s}^{-1}$), the line flux remained nearly unchanged by 2016, but then underwent a sharp increase, reaching an intensity 17 times higher than the 2016 level by 2021. After peaking concurrently with the optical brightness maximum, the flux began to decline: by 2025, it had dropped by a factor of 2.6 relative to the 2016 level. The O VI $\lambda 7082$ line emerged as a transient feature: its intensity peaked in 2021, and by 2025 the line had virtually disappeared.

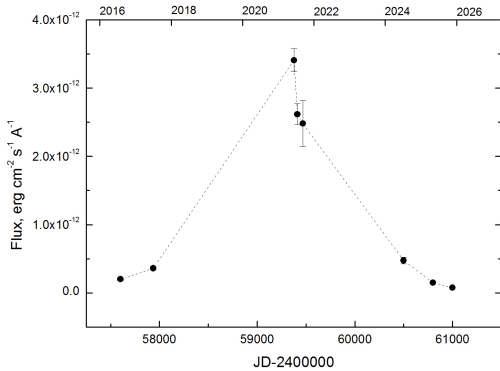


Figure 9. Temporal evolution of the absolute flux of the Raman-scattered O VI $\lambda 6825$ line from 2016 to 2025.

The behavior of the Raman-scattered lines at $\lambda 6825$ and $\lambda 7082$ serves as a direct indicator of changes in two system components: the source generating the far ultraviolet (UV) O VI resonance lines ($\lambda\lambda 1032, 1038$) – that is, the hot component or accretion disk – and the extended region of neutral hydrogen surrounding the Mira variable, where Raman scattering occurs. The 17-fold increase in flux of the $\lambda 6825$ line during 2018–2021 indicates a qualitative transition, likely caused by a sharp enhancement of accretion onto the hot component, leading to its intense heating. The coincidence of the $\lambda 6825$ flux maximum with the optical brightness peak suggests that the source of optical and UV emission (including the O VI resonance lines) is the same – the hot component of the system (WD and/or accretion disk), whose luminosity increased in both wavelength ranges. Finally, the rapid decline of the $\lambda 6825$ flux after the peak – by a factor of 2.6 by 2025 relative to the 2016 level – and the disappearance of the $\lambda 7082$ line indicate rapid fading of the ionizing source. Changes in the H I column density N_{HI} in the giant’s slow wind are a much longer-term process, making them unlikely to explain the rapid fading of the Raman lines. Interferometric observations from 2005–2006 (Sacuto et al. 2007) showed that the dusty (and therefore gaseous) envelope of the Mira variable is compact and stable on decadal timescales. The mass-loss rate of the Mira component is estimated as $\dot{M} \sim 7 \times 10^{-6} M_{\odot} \text{ yr}^{-1}$.

To substantially ($\gtrsim 50\%$) change the mean column density in such a compact envelope with characteristic size $R \sim 15$ au and wind expansion velocity $v_{\text{exp}} \sim 25 \text{ km s}^{-1}$, a timescale of order $\tau \sim R/v_{\text{exp}} \gtrsim 10\text{--}15$ yr would be required. Such a slow process cannot explain the observed rapid fading of the Raman lines over 4 years (from 2021 to 2025), confirming the dominant role of changes in the hot component rather than in the wind of the cool giant.

6.1.2. [Fe X] line

Targeted searches for the forbidden [Fe X] $\lambda 6374$ line in the optical spectrum of HM Sge were conducted during 1983–1985 (Wallerstein and Brugel 1988), using spectra with a wide dynamic range and modern detectors. The [Fe X] line was not detected in any spectrum. Wallerstein and Brugel (1988) discussed the paradox of this non-detection despite the presence of soft X-ray emission. They suggested that the ionizing radiation spectrum cuts off sharply between 100 and 300 eV, leaving insufficient photons to ionize iron to Fe^{9+} .

Subsequent studies, including our previous work (Arhipova et al. 2004), reported no [Fe X] detection in the spectrum of HM Sge. However, our 2016–2025 spectra unambiguously reveal the forbidden [Fe X] $\lambda 6374$ emission line (Tables A3 and A4). To determine when the line first appeared, we analyzed the HM Sge spectral archive from the 1.25-m telescope (2003–2015). The earliest signs of [Fe X] $\lambda 6374$ date to 2007. Due to limited data quality and challenges in absolute flux calibration, we could measure only the equivalent width (EW) of the $\lambda 6374$ line for the 2007–2015 spectra. Figure 10 and Table 3 show the EW evolution from 2007 to 2025.

From 2007 to 2017, the EW increased monotonically from ~ 6 to $\sim 34 \text{ \AA}$; by 2021 it had decreased to $\sim 13 \text{ \AA}$, and by 2025 it had dropped to minimum values ($\sim 2\text{--}3 \text{ \AA}$).

Our observations thus trace the [Fe X] line emergence in 2007, its decade-long growth, and subsequent sharp fading by 2021 – coincident with the system’s optical brightening episode of 2018–2021.

Table 3. Equivalent width of the [Fe x] $\lambda 6374$ line, 2007–2025.

Date	JD-2400000	EW (Å)	σ_{EW} (Å)
2007-06-22	54274.55	6.2	0.7
2007-08-19	54332.47	11.7	2.9
2008-07-07	54655.50	11.3	2.3
2009-06-23	55006.53	13.2	1.3
2010-08-09	55418.42	18.7	0.8
2011-08-25	55799.42	18.2	2.9
2011-09-01	55806.42	17.9	3.0
2012-07-17	56126.44	24.3	1.0
2012-07-18	56127.56	24.9	1.0
2012-07-19	56128.50	24.2	2.2
2013-07-10	56484.49	29.9	1.3
2014-07-29	56868.36	30.5	0.7
2015-07-12	57216.37	33.1	0.8
2016-07-30	57600.46	29.9	0.9
2017-07-01	57936.45	34.5	0.8
2021-06-10	59376.45	12.8	1.0
2021-07-15	59411.34	25.2	3.5
2021-09-09	59467.33	17.9	1.1
2024-07-07	60499.41	7.9	1.8
2025-05-04	60800.47	6.5	0.7
2025-08-14	60902.38	3.3	2.9
2025-11-18	60998.18	2.4	0.5

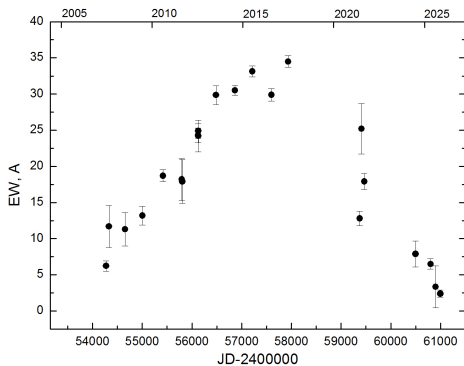


Figure 10. Temporal evolution of the equivalent width of [Fe x] $\lambda 6374$ in 2007–2025.

6.2. [O III] line formation region: gas diagnostics

Gutiérrez-Moreno et al. (1995) proposed diagnostic diagrams to distinguish planetary nebulae from symbiotic stars using intensity ratios of the forbidden [O III] lines ($\lambda\lambda 4363, 5007$) and hydrogen Balmer lines. The diagram, constructed with coordinates $R1 = I(\lambda 4363)/I(H\gamma)$

and $R2 = I(\lambda 5007)/I(H\beta)$, effectively separates planetary nebulae from symbiotic stars and distinguishes between S- and D-type symbiotics. In this diagram HM Sge lies in the D-type region. In the same work, based on observations from 1976–1988 compiled from the literature (Table 1 in Gutiérrez-Moreno et al. (1995)), the authors analyzed the temporal evolution of HM Sge’s position in the $R1$ – $R2$ plane. We extend this analysis with data from Arkhipova et al. (2004) and our 2016–2025 measurements. Figure 11 shows the object’s evolution in the $R1$ – $R2$ plane from 1976 to 2025. All values were corrected for interstellar extinction with $E(B-V) = 0.6$. Although not strictly a diagnostic diagram, in the region where HM Sge evolves ($6.0 \leq \log N_e \leq 6.5$), $R1$ is nearly independent of N_e , so its variation reflects changes in T_e alone.

Several sequential phases can be identified in the evolution of the object on the diagram over the entire observational period. First, during 1976–1988, HM Sge shifts sharply upward and to the right, corresponding to the classical outburst phase of a symbiotic nova. Physically, this is associated with a thermonuclear explosion on the WD surface, which caused a sharp increase in the temperature of the ionizing radiation source and, consequently, a moderate increase in the electron density and ionization degree of the gaseous nebula as well as its heating. Until 1986, HM Sge moves approximately along the line of constant electron density $\log N_e \approx 6.5$.

Then a downward and leftward shift begins along a broken trajectory toward a lower electron density and temperature. This phase corresponds to nebular cooling and post-outburst relaxation: as the ionizing flux declines and the nebula expands, both electron temperature and density drop significantly. During 2016–2021, the electron density increased moderately while the temperature remained stable (decreasing $R2$ at constant $R1$). Starting in 2018, a new activity phase drove HM Sge rapidly upward and rightward on the diagram – mirroring the post-1975 outburst motion, but at lower N_e values and with a more modest $R1$ increase (by a factor of ~ 2 compared to the fivefold increase earlier). Since $R1$ variations in this diagram region primarily track T_e changes, the smaller $R1$ increase during

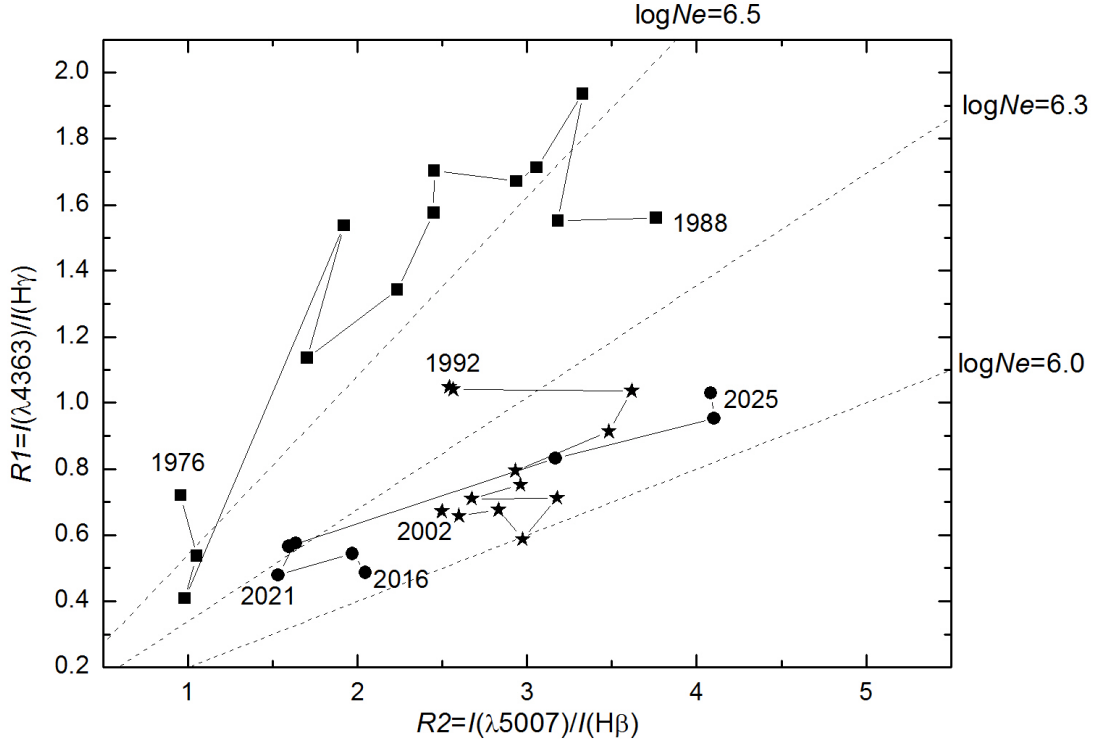


Figure 11. $R1$ – $R2$ diagram for HMSge. Squares correspond to results from Ciatti et al. (1977), Davidson et al. (1978), Blair et al. (1981), Stauffer (1984), Pacheco et al. (1989), Schmid and Schild (1990), and Pacheco and Costa (1992); stars show measurements from 1992–2002 from Arkhipova et al. (2004); circles represent our new observations from 2016–2025. Numbers on the plot indicate years. Dashed lines show contours of constant electron density $\log N_e$ in the range $6.0 \leq \log N_e \leq 6.5$ from Gutiérrez-Moreno et al. (1995).

2018–2021 indicates that the electron temperature in the [O III] line formation region rose less than it did after the 1975 outburst.

Although both activity episodes temporarily elevated electron density in the [O III] line formation region, the long-term trend across our spectroscopic monitoring shows a gradual decline. Where the object’s position in the $R1$ – $R2$ plane indicated $N_e \gtrsim 10^{6.5} \text{ cm}^{-3}$ in the 1980s, by 2025 the data align better with $N_e \gtrsim 10^6 \text{ cm}^{-3}$.

7. DISCUSSION

Based on analysis of high-ionization lines and photometric evolution, we suggest that the observed brightening of HMSge during 2018–2021

in the U , B , and V bands is likely associated with an increase in the accretion rate onto the WD. The increase in brightness in all photometric bands is probably caused by an increase in the density of ionized gas in the gas continuum formation region (free–bound and free–free), enhancing the emission as $I \propto N_e^2$. The fluxes of emission lines that contribute to the corresponding bands – He II $\lambda 4686$ in B and [Ne V], [O II] $\lambda\lambda 3727, 3729$ in U – also increased.

The evolution of the system is also manifested in the IR. Stable periodic oscillations in the $JHKLM$ bands with a period of ~ 532 days arise from pulsations of the cool Mira component. Slower variations, particularly noticeable in the J band, indicate long-term changes in the dusty envelope. The trend established af-

ter the 1975 outburst shows that the dust density reached a maximum approximately 13 years later, then gradually declined. The subsequent J -band behavior – rising to JD 2451000, declining to JD 2454500, then rising again – suggests a non-stationary process, likely related to variable dust condensation or destruction rates under the radiation field of the hot component.

The 2018–2021 high-activity episode produced significant changes in the system. By 2025, the IR brightness in all bands had declined significantly, reaching the level of the early 1990s, an epoch when the dusty envelope was densest. Although this might suggest a new episode of active dust formation, the lack of reddening in $K - L$ and $L - M$, combined with the decline $J - H$ since 2018, argues against it. Instead, the clear blueward shift in the $(J - K) - J$ color-magnitude diagram (Fig. 6) during 2019–2025 indicates altered physical conditions in the system.

We attribute these changes to enhanced UV/soft X-ray emission from the hot component during 2018–2021, which affected the compact, optically thick silicate envelope around the Mira variable (Sacuto et al. 2007). While the increased high-energy flux could not rapidly alter the envelope’s global structure (a decades-long process), it likely modified the thermal balance and grain sizes in its outer layers facing the hot source. This produced two effects: (1) heating and destruction of small grains, reducing the total IR flux; and (2) a change in the shape of near-IR continuum, decreasing the $J - H$ and $J - K$ color indices. Thus, the observed pattern reflects not new dust formation but altered conditions in the pre-existing envelope, driven by changes in the ionizing source. This scenario explains the rapid variations against a steady IR background from the Mira’s long-lived dusty wind.

Our recent spectroscopic data allow us to draw several conclusions. Nearly all emission lines in HMsge responded to the high-activity episode, including hydrogen and helium recombination lines and forbidden lines of highly ionized species. The most striking indicator of enhanced activity was the Raman-scattered O VI $\lambda 6825$ line, whose flux increased by a factor of 17 by 2021 and then rapidly declined by 2025, which

we interpret as evidence for enhanced UV output from the hot component. Contrasting variations in low- and medium-ionization lines ([O III], [N II], [S II]) – in particular, the strengthening of the [O III] $\lambda 4363$ line while the [O III] $\lambda \lambda 4959, 5007$ lines remained constant – indicate that the ionized envelope responded to the brightening episode primarily through an increase in electron density.

The [Fe X] $\lambda 6374$ line emerged in 2007 and grew through 2017 despite the fact that the optical brightness declined, which indicates that the ionizing spectrum hardened. This may reflect that the accretion disk settled into a more stationary state, where inner hot regions dominated the output. In contrast, the brightening of 2018–2021 coincided with the weakening of [Fe X] by 2021. We suggest that the higher accretion rate during this episode caused matter to accumulate on the WD surface, which expanded its outer layers and lowered the photospheric temperature. Consequently, the hard-UV flux needed to produce Fe^{+9} declined, leading to weakening of the [Fe X] line despite the increase in the system’s bolometric luminosity. This picture aligns with WD evolution models at high accretion rates (Kuuttila and Gilfanov 2021), which also explain the growth of [Fe X] in 2007–2017: the line luminosity peaks in a narrow temperature range that corresponds to stable nuclear burning (Fig. 7 in Kuuttila and Gilfanov (2021)). The observed decade-long line growth likely traces the system’s approach to this regime as the accretion disk restructured and the hardness of the ionizing radiation increased.

Outbursts are common in classical symbiotic stars and symbiotic novae. In classical symbiotic systems, they arise from enhanced accretion from the red giant, reach amplitudes of a few magnitudes, and are termed Z And-type outbursts. Such events show rapid brightening followed by a gradual return to quiescence.

Similar outbursts have also been observed in symbiotic novae: AG Peg (Skopal et al. 2017) – 165 yr after its nova-like outburst (amplitude exceeding $1^m.5$); V426 Sge (Skopal et al. 2020) – 50 yr after its outburst ($\Delta V \sim 1^m.8$). Both systems have well-defined orbital periods – 818 days for AG Peg and 493 days for V426 Sge – that per-

sist in their light curves from nova-like to Z And-type outbursts. The 2018–2021 event in HM Sge differed in several respects: smaller amplitude and no sharp brightening phase.

Moreover, the [Fe X] $\lambda 6374$ line in HM Sge behaves fundamentally differently from that observed in recurrent symbiotic novae like RS Oph. The 2010 outburst of V407 Cyg can be considered as an example, where the [Fe X] line was studied in detail throughout the event (Shore et al. 2011). In V407 Cyg, the line appeared within the first week after optical maximum (Munari et al. 2011), peaked simultaneously with X-rays (~ 40 days), and had disappeared by day 85 after the outburst. This rapid evolution is attributed to shock heating of the gas to temperatures of $\sim 1\text{--}2$ MK as the nova ejecta collide with the dense wind of the Mira variable (Shore et al. 2011), with line changes tracing the shock dynamics in an asymmetric circumstellar environment.

In HM Sge, the picture differs qualitatively. The [Fe X] line grew over ~ 10 years, peaked years before optical brightening, and then faded, inconsistent with shock excitation, which requires tight temporal correlation between coronal lines, X-rays, and optical outburst. We interpret the observed behavior as photoionization of the circumstellar environment by hard UV radiation from the accreting WD. The growth of the [Fe X] line during optical fading reflects spectral hardening as the disk restructured; subsequent weakening is associated with changes in the accretion regime and expansion of the WD atmosphere during the 2018–2021 high-activity episode.

The orbital period of HM Sge significantly exceeds typical values for classical symbiotic stars and some symbiotic novae, which may indicate a different outburst mechanism. The orbital parameters of the system, including the period, have not yet been reliably determined, and the existing estimates are contradictory. Analysis of the proper motion of the radio components N5 and S5 during 1992–1997, interpreted as motion along an elliptical orbit, yielded a separation between the binary components of ≈ 25 au and an orbital period of approximately 90 years (Richards et al. 1999). HST imaging provides

an estimate of component separation of ≈ 50 au (Eyres et al. 2001), which, within standard models, implies an orbital period of several hundred years. However, spectropolarimetry (Schmid et al. 2000) suggests a period of about 50 years, although the authors emphasize that the quality of the data is insufficient for a definitive conclusion.

If the 1975 nova-like outburst and the 2018–2021 high-activity episode both correspond to periastron passage, their ~ 46 -yr separation could approximate the orbital period. However, this hypothesis conflicts with astrometric constraints and warrants caution. The nature of the 2018–2021 event thus remains ambiguous: it may reflect enhanced periastron accretion, episodic increases in the accretion rate, or weak thermonuclear activity on the WD surface. Resolving this question will require continued multi-wavelength monitoring and high-resolution observations.

8. CONCLUSION

Analysis of photometric and spectroscopic observations of HM Sge from 2003 to 2025 yields the following conclusions:

1. After a long-term brightness decline ($\sim 0^m.05 \text{ yr}^{-1}$ from 1989 to 2017), HM Sge brightened starting in 2018 and peaked in 2021 ($\Delta V \approx 0^m.3$). By 2025, the U , B , and V brightness had fallen to the faintest levels in five decades of monitoring. This indicates that after the 2018–2021 high-activity episode, the system has not returned to its pre-brightening state but has continued its evolution with altered parameters.

2. Near-IR observations confirm Mira-type pulsations with a period of 532 days. During the 2018–2021 optical brightening, IR emission remained largely unchanged except for a modest J -band increase. After 2021, all bands (J , H , K , L , M) faded monotonically, reaching early-1990s levels by 2025 – when the dusty envelope was densest after the 1975 outburst. The absence of reddening in $K-L$ and $L-M$, combined with bluer $J-H$ and $J-K$ color indices since 2019, rules out new dust formation. Instead, we attribute these changes to the heating and de-

struction of small dust grains by enhanced UV radiation from the hot component.

3. The 2018–2021 high-activity episode produced significant spectral changes: the fluxes of recombination lines (H I, He I, He II) and high-excitation forbidden lines ([Ar V], [Fe VI], [Fe VII]) increased. The [Fe X] λ 6374 line, detected in HM Sge for the first time, began growing in 2007 and peaked in 2017 – several years before the optical maximum. This timeline indicates photoionization by hard UV radiation from a source (accretion disk or WD) that restructured well before the optical brightening. The [Fe X] flux declined after 2021, tracking the hot component’s fading activity. This behavior matches models, where high accretion rates expand the WD’s outer layers and lower its photospheric temperature (Kuuttila and Gilfanov 2021).

4. The flux of the Raman-scattered O VI λ 6825 line increased 17-fold during 2018–2021, directly tracing enhanced ionizing radiation from the hot component. The system’s position on the [O III] diagnostic diagram shifted toward higher electron temperatures, marking the onset of a new heating cycle in the gaseous envelope.

5. We interpret the 2018–2021 event as resulting from enhanced accretion from the red giant

onto the WD. The 1975 outburst and 2018–2021 episode may both correspond to periastron passage; if so, the \sim 46-yr interval would approximate the orbital period. However, this hypothesis requires further verification.

This paper presents a qualitative analysis of new observational data for HM Sge from 2003 to 2025. Our results reveal substantial changes in the photometric and spectral behavior of the system. However, a more complete understanding of the underlying physical processes will require quantitative modeling. In future work, we plan to determine fundamental system parameters and simulate the spectral energy distribution, accounting for contributions from various system components.

HM Sge remains a unique laboratory for studying the late stages of symbiotic nova evolution. Clarifying the processes driving recurrent heating and long-period activity will require further observations across all accessible wavelength ranges.

ACKNOWLEDGMENTS

The study was conducted under the state assignment of the Lomonosov Moscow State University.

-
- D. A. Allen, *Proceedings of the Astronomical Society of Australia* **5** (3), 369 (1984).
 V. P. Arkhipova, O. D. Dokuchaeva, and V. F. Esipov, *Soviet Astronomy* **23** (2), 174 (1979).
 V. P. Arkhipova, O. D. Dokuchaeva, and R. I. Noskova, *Astronomy Letters* **20** (5), 623 (1994).
 V. P. Arkhipova, V. F. Esipov, N. P. Ikonnikova, and R. I. Noskova, *Astronomy Letters* **30**, 258 (2004).
 V. P. Arkhipova and R. I. Noskova, *Soviet Astronomy Letters* **17**, 188 (1991).
 C. A. L. Bailer-Jones, J. Rybizki, M. Fouesneau, et al., *Astronomical Journal* **161** (3), 147 (2021).
 W. P. Blair, R. E. Stensel, G. Shaviv, and W. A. Feibelman, *Astronomy and Astrophysics* **99**, 239 (1981).
 L. W. Brown, W. A. Feibelman, R. W. Hobbs, and C. W. McCracken, *Astrophysical Letters* **19**, 75 (1978).
 F. Ciatti, A. Mammano, and A. Vitone, *Astronomy and Astrophysics* **61**, 459 (1977).
 F. Ciatti, A. Mammano, and A. Vitone, *Astronomy and Astrophysics* **68**, 251 (1978).
 K. Davidson, R. M. Humphreys, and K. M. Merrill, *Astrophysical Journal* **220**, 239 (1978).
 O. D. Dokuchaeva, *Information Bulletin on Variable Stars* **1189**, 1 (1976).
 S. P. S. Eyres, M. F. Bode, A. R. Taylor, et al., *Astrophysical Journal* **551**, 512 (2001).
 Gaia Collaboration, A. G. A. Brown, A. Vallenari, et al., *Astronomy and Astrophysics* **649**, A1 (2021).
 S. R. Goldman, R. Sankrit, E. Montiel, et al., *Astrophysical Journal* **961** (1), 14 (2024).

- A. Gutiérrez-Moreno, H. Moreno, and G. Cortes, *Publications of the Astronomical Society of the Pacific* **107**, 462 (1995).
- A. P. Ipatov and B. F. Yudin, *Soviet Astronomy Letters* **7**, 309 (1981).
- H. L. Johnson, R. I. Mitchel, B. Iriarte, and W. Z. Wisniewski, *Communications of the Lunar and Planetary Laboratory* **4**, 99 (1966).
- J. Kuuttila and M. Gilfanov, *Monthly Notices of the Royal Astronomical Society* **507** (1), 594 (2021).
- H.-W. Lee and S. Kang, *Astrophysical Journal* **669**, 1156 (2007).
- H.-W. Lee, D.-S. Lee, S.-J. Chang, et al., *Astrophysical Journal* **833**, 75 (2016).
- V. M. Lyutyj, *Soobshcheniya Gosudarstvennogo Astronomicheskogo Instituta* **172**, 30 (1971). In Russian.
- U. Munari, V. H. Joshi, N. M. Ashok, et al., *Monthly Notices of the Royal Astronomical Society* **410** (1), L52 (2011).
- U. Mürset and H. Nussbaumer, *Astronomy and Astrophysics* **282**, 586 (1994).
- U. Mürset and H. M. Schmid, *Astronomy and Astrophysics Supplement Series* **137**, 473 (1999).
- A. E. Nadjip, V. I. Shenavrin, and V. G. Tichonov, *Trudy Gosudarstvennogo Astronomicheskogo Instituta* **58**, 119 (1986).
- R. I. Noskova, *Astronomy Letters* **22** (6), 755 (1996).
- H. Nussbaumer and M. Vogel, *Astronomy and Astrophysics* **236**, 117 (1990).
- J. A. F. Pacheco, S. J. Codina-Landaberry, and D. F. Lopes, *Astrophysical Journal* **337**, 520 (1989).
- J. A. F. Pacheco and R. D. D. Costa, *Astronomy and Astrophysics* **257**, 619 (1992).
- S. A. Potanin, A. A. Belinski, A. V. Dodin, et al., *Astronomy Letters* **46** (12), 836 (2020).
- R. C. Puetter, R. W. Russell, B. T. Soifer, and S. P. Willner, *Astrophysical Journal* **223**, L93 (1978).
- A. M. S. Richards, M. F. Bode, S. P. S. Eyres, et al., *Monthly Notices of the Royal Astronomical Society* **305**, 380 (1999).
- S. Sacuto, O. Chesneau, M. Vannier, and P. Cruzalèbes, *Astronomy and Astrophysics* **465**, 469 (2007).
- H. M. Schmid, R. Corradi, J. Krautter, and H. Schild, *Astronomy and Astrophysics* **355**, 261 (2000).
- H. M. Schmid and H. S. Schild, *Monthly Notices of the Royal Astronomical Society* **246**, 84 (1990).
- G. I. Shanin, *Soviet Astronomy Letters* **4**, 100 (1978).
- V. I. Shenavrin, O. G. Taranova, and A. E. Nadzhip, *Astronomy Reports* **55** (1), 31 (2011).
- S. N. Shore, G. M. Wahlgren, T. Augusteijn, et al., *Astronomy and Astrophysics* **527**, A98 (2011).
- A. Skopal, S. Y. Shugarov, U. Munari, et al., *Astronomy and Astrophysics* **636**, A77 (2020).
- A. Skopal, S. Y. Shugarov, M. Sekeráš, et al., *Astronomy and Astrophysics* **604**, A48 (2017).
- J. R. Stauffer, *Astrophysical Journal* **280**, 695 (1984).
- O. G. Taranova and V. I. Shenavrin, *Astronomy Letters* **26**, 600 (2000).
- O. G. Taranova and B. F. Yudin, *Astronomy and Astrophysics* **117**, 209 (1983).
- G. Wallerstein and E. Brugel, *Astronomy and Astrophysics* **197**, 182 (1988).
- B. Yudin, U. Munari, O. Taranova, and I. Dalmeri, *Astronomy and Astrophysics Supplement Series* **105**, 169 (1994).
- B. F. Yudin, *Astronomy Reports* **38** (6), 801 (1994).

APPENDIX

Table A1: *UBV* photometry for HM Sge, 2003–2025.

JD-2400000	<i>U</i>	<i>B</i>	<i>V</i>
57213	12.14	13.09	12.56
57216	12.11	13.05	12.53
57217	12.12	13.09	12.50
57249	12.13	13.08	12.51
57272	12.12	13.07	12.53
57299	12.15	13.10	12.54
57517	12.20	13.15	12.57
57549	12.23	13.13	12.60
57573	12.16	13.11	12.53
57584	12.17	13.12	12.54
57638	12.25	13.12	12.55
57640	12.23	13.15	12.55
57935	12.23	13.19	12.59
57958	12.26	13.17	12.59
57959	12.29	13.21	12.56
57980	12.33	13.18	12.57
58013	12.28	13.20	12.60
58341	12.16	13.05	12.45
58344	12.19	13.05	12.46
58351	12.18	13.04	12.45
58366	12.16	13.04	12.45
58600	12.04	12.95	12.40
58607	12.03	12.94	12.41
58617	12.04	12.92	12.38
58635	12.02	12.90	12.37
58638	12.04	12.93	12.39
58647	12.00	12.92	12.39
58658	12.04	12.89	12.36
58661	11.99	12.90	12.37
58677	12.00	12.90	12.34
58672	12.02	12.91	12.37
58691	12.00	12.90	12.34
58701	11.99	12.89	12.37
58704	12.00	12.92	12.36
58719	12.00	12.88	12.34
58729	12.01	12.89	12.36
58730	12.00	12.91	12.35
58753	12.00	12.91	12.36
58760	12.01	12.88	12.36
59043	12.03	12.90	12.32
59060	12.00	12.90	12.33
59078	11.99	12.93	12.33
59079	12.01	12.90	12.36
59087	12.00	12.86	12.35
59110	11.98	12.90	12.34
59145	11.98	12.92	12.38
59339	11.92	12.88	12.33
59374	11.94	12.86	12.28
59377	11.92	12.85	12.27

JD-2400000	<i>U</i>	<i>B</i>	<i>V</i>
59410	11.94	12.84	12.27
59429	11.94	12.85	12.26
59339	11.92	12.88	12.33
59374	11.94	12.86	12.28
59377	11.92	12.85	12.27
59410	11.94	12.84	12.27
59429	11.94	12.85	12.26
59732	12.10	13.03	12.44
59760	12.06	13.03	12.45
59765	12.08	13.05	12.47
59766	12.05	13.04	12.46
59787	12.07	13.07	12.47
59796	12.04	13.06	12.46
59821	12.10	13.14	12.55
59732	12.10	13.03	12.44
59765	12.08	13.05	12.47
59766	12.05	13.04	12.46
59787	12.07	13.07	12.48
59796	12.04	13.06	12.46
59851	12.10	13.14	12.55
60083	12.32	13.39	12.76
60116	12.36	13.39	12.70
60120	12.37	13.42	12.73
60208	12.45	13.49	12.76
60223	12.43	13.51	12.80
60469	12.53	13.62	12.84
60494	12.51	13.62	12.87
60534	12.58	13.67	12.91
60536	12.54	13.68	12.95
60863	12.84	14.04	13.13
60877	12.82	13.99	13.14
60878	12.80	13.98	13.11

Table A2: *JHKLM* photometry for HM Sge, 2009-2025.

JD-2400000	<i>J</i>	<i>H</i>	<i>K</i>	<i>L</i>	<i>M</i>
54982.5	8.34	6.38	4.56	2.33	1.65
54994.5	8.32	6.31	4.49	2.26	1.65
55014.4	8.02	6.07	4.27	2.09	1.58
55021.4	7.91	5.99	4.16	1.98	1.49
55047.4	7.59	5.69	3.92	1.78	1.20
55056.4	7.51	5.64	3.89	1.76	1.20
55113.2	7.20	5.44	3.72	1.66	1.20
55145.1	7.10	5.30	3.68	1.65	1.15
55318.5	7.87	5.97	4.28	2.16	1.63
55408.4	8.50	6.48	4.65	2.44	1.91
55431.3	8.51	6.50	4.62	2.43	1.76
55434.3	8.44	6.44	4.65	2.42	1.81
55463.2	8.44	6.38	4.57	2.38	1.73
55493.2	8.29	6.28	4.50	2.31	1.73
55503.2	8.20	6.21	4.44	2.28	1.75
55692.5	6.95	5.21	3.64	1.64	1.06
55729.5	6.95	5.24	3.68	1.68	1.31

JD-2400000	<i>J</i>	<i>H</i>	<i>K</i>	<i>L</i>	<i>M</i>
55751.4	7.01	5.31	3.74	1.71	1.14
55759.5	7.08	5.34	3.75	1.73	1.26
55780.4	7.22	5.49	3.87	1.82	1.30
55784.4	7.26	5.50	3.90	1.86	1.34
55794.4	7.34	5.55	3.96	1.89	1.37
55811.3	7.49	5.70	4.06	1.99	1.42
55820.3	7.57	5.77	4.10	2.02	1.54
55843.2	7.84	5.96	4.26	2.14	1.53
55870.2	8.05	6.16	4.41	2.26	1.66
56059.5	8.20	6.25	4.39	2.21	1.73
56084.5	7.91	6.04	4.27	2.11	1.60
56092.5	7.74	5.91	4.17	2.04	1.51
56111.4	7.42	5.67	3.96	1.88	1.35
56136.4	7.20	5.50	3.83	1.78	1.13
56197.3	6.97	5.29	3.69	1.68	1.05
56224.2	6.94	5.19	3.62	1.69	1.06
56434.5	8.23	6.28	4.52	2.37	1.81
56470.5	8.35	6.41	4.61	2.47	1.95
56473.4	8.38	6.42	4.61	2.49	1.92
56485.5	8.42	6.42	4.64	2.48	1.98
56497.4	8.46	6.46	4.65	2.49	1.96
56518.4	8.40	6.42	4.63	2.43	1.84
56579.2	8.32	6.34	4.53	2.38	1.78
56824.5	7.12	5.33	3.74	1.76	1.27
56848.4	7.16	5.34	3.77	1.81	1.35
56875.4	7.18	5.41	3.84	1.88	1.32
56883.4	7.24	5.45	3.89	1.92	1.47
56914.3	7.42	5.57	4.02	2.11	1.57
56937.2	7.63	5.77	4.18	2.16	1.55
56967.2	7.86	5.97	4.33	2.30	1.70
57205.4	7.35	5.60	3.91	1.87	1.33
57234.4	7.20	5.48	3.85	1.81	1.33
57261.4	7.14	5.44	3.81	1.79	1.28
57268.3	7.10	5.40	3.78	1.78	1.25
57287.3	6.98	5.28	3.68	1.70	1.25
57525.5	7.88	6.12	4.48	2.46	1.93
57561.5	7.91	6.14	4.54	2.47	2.03
57584.4	7.90	6.14	4.52	2.46	1.90
57592.4	7.88	6.12	4.51	2.46	2.02
57618.4	7.85	6.06	4.45	2.40	1.94
57637.4	7.81	6.05	4.44	2.44	1.94
57646.3	7.76	6.03	4.42	2.39	1.83
57916.5	6.91	5.33	3.90	1.94	1.44
57943.5	6.98	5.43	4.04	2.06	1.47
57968.5	7.10	5.55	4.14	2.23	1.73
57973.4	7.06	5.51	4.14	2.22	1.76
58000.4	7.20	5.66	4.22	2.34	1.78
58242.6	7.25	5.72	4.27	2.33	1.89
58303.5	6.81	5.39	4.04	2.11	1.71
58330.4	6.75	5.37	4.00	2.05	1.69
58352.4	6.73	5.36	3.97	2.07	1.49
58363.4	6.72	5.35	3.96	2.04	1.60
58386.2	6.71	5.32	3.95	2.02	1.56

JD-2400000	<i>J</i>	<i>H</i>	<i>K</i>	<i>L</i>	<i>M</i>
58415.2	6.78	5.33	4.00	2.08	1.54
58448.1	6.76	5.36	4.01	2.10	1.6
58631.5	7.66	6.05	4.58	2.66	–
58653.5	7.70	6.08	4.61	2.66	2.02
58678.4	7.71	6.10	4.61	2.67	2.18
58709.3	7.72	6.08	4.55	2.59	1.98
58721.3	7.68	6.09	4.55	2.58	2.06
58736.3	7.73	6.11	4.58	2.60	2.00
58766.3	7.69	6.07	4.54	2.56	2.05
58797.2	7.38	5.86	4.35	2.35	1.78
58972.5	6.96	5.58	4.17	2.17	1.60
59026.5	7.13	5.73	4.30	2.32	1.76
59041.4	7.24	5.79	4.41	2.38	1.84
59060.4	7.31	5.90	4.46	2.44	2.02
59076.4	7.37	5.93	4.52	2.44	1.79
59095.3	7.51	6.03	4.57	2.56	1.99
59124.2	7.72	6.20	4.70	2.68	2.14
59166.2	7.89	6.31	4.78	2.77	2.23
59376.5	6.94	5.55	4.10	2.15	1.66
59386.4	6.89	5.52	4.08	2.13	1.70
59415.5	6.83	5.43	3.98	2.04	1.56
59444.5	6.79	5.39	4.00	2.02	1.53
59452.3	6.82	5.43	3.99	2.06	1.58
59517.2	6.94	5.52	4.08	2.12	1.60
59768.4	8.22	6.48	4.86	2.79	2.22
59780.4	8.20	6.47	4.83	2.79	2.24
59867.2	7.72	6.15	4.61	2.61	2.08
59893.2	7.39	5.89	4.39	2.38	1.87
60123.5	7.50	5.84	4.33	2.34	1.84
60154.4	7.74	6.08	4.52	2.14	2.02
60184.4	7.94	6.30	4.71	2.66	2.26
60211.2	8.16	6.45	4.84	2.74	2.23
60247.2	8.39	6.64	4.99	2.91	2.30
60447.5	7.40	5.87	4.32	2.28	1.82
60462.4	7.24	5.74	4.21	2.20	1.80
60485.5	7.08	5.61	4.10	2.12	1.66
60512.4	7.07	5.57	4.06	2.12	1.71
60538.4	7.04	5.52	4.05	2.04	1.61
60567.3	7.04	5.51	4.05	2.08	1.66
60622.2	7.13	5.61	4.15	2.17	1.81
60818.5	8.68	6.96	5.31	3.08	2.57
60833.5	8.75	7.00	5.34	3.06	2.56

Table A3: Absolute emission line fluxes in the spectrum of HM Sge from observations obtained with the 1.25-m telescope. Fluxes are given in units of 10^{-13} erg cm $^{-2}$ s $^{-1}$.

λ_{lab} (Å)	Ion	$F(2016-07-30)$	$F(2017-07-01)$	$F(2021-07-15)$	$F(2021-09-09)$	$F(2024-07-07)$
4101.76	H I	8.01	7.60	12.06	12.23	–
4340.47	H I	16.67	15.46	23.98	20.30	12.46
4363.21	[O III]	8.21	8.51	13.99	11.63	10.50
4416.5bl	[Fe II]	–	–	2.36	1.92	–
4471.48	He I	0.63	0.51	2.00	1.93	–
4541.59	He II	0.96	1.03	2.53	2.38	–
4582.83	Fe II	–	1.22	–	–	–
4685.68	He II	35.66	35.17	60.86	51.12	27.78
4861.33	H I	50.29	49.98	68.31	56.82	34.05
4940.68	–	7.88	8.12	10.58	8.41	8.40
4958.92	[O III]	41.08	40.38	45.43	38.60	43.67
5006.84	[O III]	125.90	120.50	136.70	110.90	131.90
5145.75	[Fe VI]	0.82	0.67	1.21	1.31	1.49
5158.01	[Fe II]	1.65	2.07	5.98	5.25	3.11
5176.04	[Fe VI]	1.60	1.86	3.51	3.51	2.97
5197.90	[N II]	0.38	0.53	1.58	1.47	–
5234.28	[Fe VI]	0.22	–	1.57	–	0.35
5275.82	[Ni II]	1.97	2.25	5.76	4.73	3.38
5309.02	[Ca V]	1.38	1.95	5.45	4.90	2.61
5335.18	[Fe VI]	–	0.54	2.50	2.24	0.64
5412.00	He II / [Fe III]	4.45	4.70	7.93	6.78	3.39
5427.82	[Fe II]	–	–	–	–	0.63
5460.50	Fe II	–	–	–	0.75	0.46
5619.00	[Ca VII]	6.94	6.85	11.18	10.30	7.54
5631.07	[Fe VI]	–	–	–	–	0.62
5676.95	[Fe VI]	–	–	–	–	0.57
5721.15	[Fe VII]	10.39	10.90	17.00	16.20	18.00
5754.64	[N II]	4.39	4.42	4.10	3.65	3.01
5875.67	He I	4.53	4.65	8.77	8.09	4.17
6086.92	[Fe VII]	18.92	19.75	29.02	27.05	30.82
6300.30	[O I]	7.15	8.13	11.16	10.28	4.70
6312.06	[S III]	3.75	4.26	3.75	3.68	3.04
6363.78	[O I]	2.45	2.41	3.80	3.61	1.56
6374.53	[Fe X]	4.12	5.94	4.05	3.52	0.67
6435.10	[Ar V]	2.01	2.46	3.50	3.31	1.98
6548.03	[N II]	–	–	31.44	24.70	19.32
6562.82	H I	329.90	404.70	511.00	473.70	209.10
6583.45	[N II]	45.72	59.32	56.11	53.78	51.34
6678.15	He I	1.68	1.89	4.01	3.68	1.62
6716.47	[S II]	1.45	1.58	1.63	1.73	2.11
6730.85	[S II]	2.71	3.24	3.46	3.41	4.13
6825.00	O VI	2.01	3.59	26.16	24.80	4.74
6891.00	He II	0.87	0.87	1.19	1.18	0.64
7005.83	[Ar V]	5.29	5.39	5.54	5.06	4.07
7065.28	He I	4.19	4.28	9.60	8.70	3.56
7135.78	[Ar III]	9.32	8.69	8.47	8.07	8.16
7155.17	[Fe II]	0.64	0.96	4.41	3.93	1.25
7171.62	[Ar IV]	0.84	1.77	–	3.26	1.07
7237.17	C II	0.69	0.65	–	0.72	0.70
7263.33	[Ar IV]	0.61	0.59	–	0.53	0.57

Continuation of Table A3. Absolute fluxes are given in units of 10^{-13} erg cm $^{-2}$ s $^{-1}$.

λ_{lab} (Å)	Ion	$F(2016-07-30)$	$F(2017-07-01)$	$F(2021-07-15)$	$F(2021-09-09)$	$F(2024-07-07)$
7281.35	He I	0.50	–	–	0.90	–
7291.00	–	–	–	–	1.11	–
7319.40	[O II]	7.47	8.10	7.34	6.27	5.41
7330.70	[O II]	6.22	5.50	5.52	4.62	4.68
7377.83	[Ni II]	–	0.53	2.36	1.93	0.85
7388.40	[Fe II]	–	–	1.22	1.04	0.38
7411.61	[Ni II]	–	–	0.83	0.75	0.27
7452.56	[Fe II]	–	0.29	1.29	1.34	0.35
7530.83	[Cl IV]	0.72	0.27	–	–	0.22
7593.00	–	2.65	3.17	1.95	2.44	2.37
7712.28	Fe II	2.13	2.60	3.31	3.81	–
7751.43	[Ar III]	2.36	2.55	1.72	1.72	2.10
7866.56	Fe II	–	0.39	1.71	–	–
7967.00	–	2.10	2.29	–	–	–
8046.10	[Cl IV]	0.62	0.65	–	–	0.62
8237.92	Fe II	3.00	2.52	–	–	–
8445.00	O I	5.02	9.53	–	–	–
8467.26	H I	0.72	–	–	–	–
8502.49	H I	0.79	–	–	–	–
8545.38	H I	0.96	–	–	–	–
8598.39	H I	1.23	–	–	–	–
8665.02	H I	1.53	–	–	–	–
8750.48	H I	1.74	–	–	–	–
8862.79	H I	2.31	–	–	–	–
8926.66	Fe II	1.54	–	–	–	–
9014.91	H I	4.36	–	–	–	–
9068.60	[S III]	–	15.13	–	–	15.09
9530.60	[S III]	–	41.99	–	–	–

Table A4: Absolute emission line fluxes in the spectrum of HMsge from observations obtained with the TDS spectrograph. Fluxes are given in units of 10^{-13} erg cm $^{-2}$ s $^{-1}$.

λ_{lab} (Å)	Ion	$F(2021-06-10)$	$F(2025-05-04)$	$F(2025-11-18)$
3585.99	–	7.77	8.16	8.28
3727.50	[O II]bl	6.35	5.65	4.78
3757.40	[Fe VI]	12.39	11.18	11.82
3835.40	H I	4.38	–	–
3868.76	[Ne III]	18.60	16.67	17.35
3889.02	H I+He I	8.13	3.65	3.65
3968.72	[Ne III]+H I	14.60	8.39	8.64
4068.60	[S II]	3.84	2.15	2.16
4076.35	[S II]	1.10	0.72	0.76
4101.76	H I	14.58	5.47	5.29
4199.10	He II	2.59	0.94	0.72
4246.23	Fe II	4.11	1.16	0.89
4340.47	H I	25.20	9.94	9.54
4363.21	[O III]	12.21	9.60	9.95
4416.50	[Fe II]bl	2.84	0.29	0.26
4471.48	He I	2.01	0.67	0.68

Continuation of Table A4. Absolute fluxes are given in units of 10^{-13} erg cm $^{-2}$ s $^{-1}$.

λ_{lab} (Å)	Ion	F (2021-06-10)	F (2025-05-04)	F (2025-11-18)
4541.59	He II	2.36	0.70	0.65
4582.83	Fe II	2.84	0.31	0.16
4634.14	N III	1.71	0.53	0.50
4640.64	N III	3.42	1.15	0.99
4656.98	Fe II	1.05	0.57	0.59
4685.68	He II	60.32	23.20	23.16
4698.82	[Fe VII]	0.91	0.88	0.99
4713.14	He I	1.71	1.17	1.14
4725.62	[Ne IV]	2.31	1.30	1.25
4740.12	[Ar IV]	1.08	1.20	1.26
4774.73	[Fe II]	0.20	–	–
4814.54	[Fe II]	1.15	–	–
4861.33	H I	68.43	29.50	29.61
4891.57	–	4.61	1.51	1.63
4940.68	[Ca VII]	9.48	5.34	5.10
4958.92	[O III]	40.17	48.50	48.24
4988.40	[Fe VII]	1.40	1.71	1.88
5006.84	[O III]	128.10	148.00	147.90
5145.75	[Fe VI]	1.18	1.35	1.55
5158.01	[Fe II]	5.37	2.79	2.94
5176.04	[Fe VI]	2.85	2.77	2.94
5197.90	[N I]	1.66	0.26	0.30
5275.82	[Ni II]	3.85	2.76	2.86
5309.11	[Ca V]	2.66	2.27	2.41
5316.77	Fe II	2.65	–	–
5411.48	He II	7.60	2.41	2.15
5425.27	Fe II	0.73	–	–
5527.35	[Fe II]	0.98	–	–
5534.89	Fe II	0.99	–	–
5577.34	[O I]	0.49	0.07	0.08
5618.75	[Ca VII]	11.10	5.43	4.78
5631.07	[Fe VI]	0.62	–	–
5676.95	[Fe VI]	0.48	0.59	0.72
5721.15	[Fe VII]	19.16	16.20	19.11
5754.64	[N II]	4.38	2.85	2.94
5875.67	He I	10.10	3.31	3.33
6086.92	[Fe VII]	33.17	28.50	27.43
6300.30	[O I]	13.47	3.58	3.55
6312.06	[S III]	4.21	2.69	2.83
6363.78	[O I]	4.55	1.19	1.20
6374.53	[Fe X]	3.63	0.21	0.11
6435.10	[Ar V]	4.33	1.63	1.71
6416.93	Fe II	0.93	–	–
6455.15	Fe II	2.61	–	–
6548.03	[N II]	17.06	17.20	17.17
6562.82	H I	608.70	167.00	166.80
6583.45	[N II]	52.80	51.70	51.74
6666.87	[Ni II]	0.66	0.06	0.08
6678.15	He I	3.95	0.95	0.95
6683.21	He II	0.99	0.27	0.21
6716.47	[S II]	1.69	1.66	1.68

Continuation of Table A4. Absolute fluxes are given in units of 10^{-13} erg cm $^{-2}$ s $^{-1}$.

λ_{lab} (\AA)	Ion	F (2021-06-10)	F (2025-05-04)	F (2025-11-18)
6730.85	[S II]	4.09	3.39	3.52
6825.00	O VI	34.07	1.51	0.77
6890.80	He II	1.08	0.36	0.37
7005.83	[Ar V]	6.08	3.72	4.10
7065.28	He I	11.84	2.63	2.55
7087.85	O VI	5.21	–	–
7135.78	[Ar III]	9.90	7.22	7.63
7155.17	[Fe II]	5.36	0.63	0.63
7237.17	C II	0.90	0.56	0.58
7291.00	–	0.78	–	–
7319.40	[O II]	6.76	4.07	4.18
7330.83	[O II]	5.34	3.31	3.73
7377.83	[Ni II]	2.79	0.37	0.39
7388.40	[Fe II]	1.03	0.10	0.49
7411.61	[Ni II]	1.10	–	–
7452.56	[Fe II]	1.31	–	0.26